10/10/99-6:04 PM
Report No. UCB/R/99/A1166

Department of Materials Science and Mineral Engineering
University of California at Berkeley

ROLE OF FOREIGN OBJECT DAMAGE ON THRESHOLDS FOR HIGH-CYCLE FATIGUE IN Ti-6Al-4V

J. O. Peters,[1] O. Roder,[1,2] B. L. Boyce,[1] A. W. Thompson,[1] and R. O. Ritchie[1]

[1]Department of Materials Science and Mineral Engineering,
University of California, Berkeley, CA 94720-1760, U.S.A.

[2]currently at Daimler Chrysler Aerospace - MTU Munich, 80976 Munich, Germany

July 1999

submitted to
Metallurgical and Materials Transactions A

Work supported by the Air Force Office of Scientific Research, Grant No. F49620-96-1-0478 under the auspices of the Multidisciplinary University Research Initiative on *High Cycle Fatigue* to the University of California.

ROLE OF FOREIGN OBJECT DAMAGE ON THRESHOLDS FOR HIGH-CYCLE FATIGUE IN Ti-6Al-4V

J. O. Peters, O. Roder,[*] B. L. Boyce, A. W. Thompson, and R. O. Ritchie
Department of Materials Science and Mineral Engineering,
University of California, Berkeley, CA 94720-1760, U.S.A.

ABSTRACT

The increasing incidence of military aircraft engine failures that can be traced to high-cycle fatigue (HCF) has prompted a reassessment of the design methodologies for HCF-critical components, such as turbine blades and disks. Because of the high-frequency vibratory loading involved, damage-tolerant design methodologies based on a threshold for no crack growth offer a preferred approach. As impact damage from ingested debris is a prime source of HCF-related failures, the current study is focused on the role of such foreign object damage (FOD) in influencing fatigue-crack growth thresholds and early crack growth of both large and small cracks in a fan blade alloy, Ti-6Al-4V. FOD, which was simulated by the high-velocity (200-300 m/s) impacts of steel spheres on a flat surface, was found to reduce markedly the fatigue strength, primarily due to earlier crack initiation. This is discussed in terms of four salient factors: (i) the stress concentration associated with the FOD indentation, (ii) the presence of small microcracks in the damaged zone, (iii) the localized presence of tensile residual hoop stresses at the base and rim of the indent sites, and (iv) microstructural damage from FOD-induced plastic deformation. It was found that no crack growth occurred from FOD impact sites in this alloy at ΔK values below ~2.9 MPa√m, i.e., over 50% higher than the "closure-free", *worse-case* threshold value of ΔK_{TH} = 1.9 MPa√m, defined for large cracks in bimodal Ti-6Al-4V at the highest possible load ratio. It is therefore concluded that such worst-case, large-crack thresholds can thus be used as a practical lower-bound to FOD-initiated cracking in this alloy.

[*] Currently at Daimler Chrysler Aerospace - MTU Munich, 80976 Munich, Germany

I. INTRODUCTION

The increasing incidence of high cycle fatigue (HCF) related failures of gas turbine engines in military aircraft has led to a re-evaluation of the current Goodman design approach for HCF.[1-3] Larsen *et al.*,[3] for example, have reviewed the limitations of the Goodman approach and concluded that it does not account explicitly for such critical factors as interactions of low cycle fatigue (LCF) and HCF loading, or the microstructural variability and surface damage, e.g., due to fretting or foreign object damage, which can act as potential sources for crack initiation under the high-frequency, in-service vibratory loading. Indeed, because of the high frequencies (>1 kHz) involved, any degree of crack growth could potentially result in failure during operation; consequently, to avoid HCF failures, the design of critical components should involve a damage-tolerant methodology,[1-4] specifically based on the concept of a fatigue-crack growth threshold, defined under representative HCF conditions of high frequencies, high load ratios and small crack sizes.

Foreign object damage (FOD) is a prime cause of such HCF failures. The term is used to indicate damage from bird strikes and hard body impacts, such as stones, striking primarily the turbine engine fan blades when ingested with the airflow.[5,6] Depending on the impact conditions, FOD can result in the immediate separation of a blade, or can cause sufficient microstructural damage, stress-raising notches and even cracks, which induce the early initiation of fatigue cracks. Since fan and compressor blades can experience in service transient airflow dynamics, from resonant conditions of the engine, in the form of low amplitude airfoil excitations in the kHz-regime (and, depending on the blade span location, very high mean stress levels), such premature cracking can result in essentially unpredictable failures due to fatigue-crack growth in very short time periods.[2,3]

To develop a predictive, mechanism-based model for the role of FOD in inducing HCF failures, a key aspect is to characterize how FOD affects the HCF thresholds. This involves assessing the effect of stress concentration, FOD-induced microcracking, residual stress gradients,[2,7,8] and the microstructural changes due to the FOD-induced plastic deformation.[9,10] It is the objective of the present study to examine this role of FOD, simulated by normal high-

velocity impacts of small steel spheres on the flat surfaces of fatigue test specimens, in influencing the fatigue crack-growth thresholds and near-threshold crack-growth rates in a Ti-6Al-4V alloy processed for typical turbine blade applications.

II. BACKGROUND

A. *Stress Concentration*

Traditional design approaches for HCF, based on a modified Goodman diagram, assess the role of FOD in terms of the effective-fatigue stress concentration factor (k_f), i.e., the ratio of the fatigue limit of a smooth component to that of a FOD-notched component.[6] Whereas the HCF life of blunt notches is dominated by crack initiation and can generally be predicted using the elastic stress concentration factor (k_t), for sharp notches the HCF strength approaches a lower limiting value which can be expressed in terms of k_f. The existence of a critical notch sharpness in affecting the fatigue limit is attributed to the initiation, growth and subsequently arrest of small cracks at sharp notches under the influence of high notch-stress gradient at nominally low stresses.[11-13] To incorporate these effects into a design for HCF, Hudak *et al*.[7] have proposed a "worst case notch" concept based on a fatigue-crack growth threshold that accounts for the statistical severity of FOD-induced notches.

B. *FOD-Induced Cracking*

In brittle alloys, such as gamma titanium aluminides, FOD-like impact damage can result in extensive microcracking within the damaged region, which provides the prime reason for the degradation in fatigue life of these alloys due to FOD.[14] However, in more ductile materials such as Ti-6Al-4V, reports of microcracking in the vicinity of damage sites are rare. The presence of such microcracks, however, is of critical importance as it provides a very potent site for HCF cracks to initiate.

C. *Residual Stresses*

In addition to the geometrical effects of the impact sites, FOD induces residual stresses in the vicinity of these sites, which can have a profound influence on the location and conditions for

crack initiation.[2,8,9,15] Unfortunately, numerical and experimental analyses of dynamic and quasi-static indentation loading available in the literature,[9,16-23] which simulate simple-geometry FOD by indenting spherical steel indenter often onto steel target, do not provide consistent residual stress fields with respect to the primary fatigue crack initiation sites at the indent base and rim locations. For example, dynamic indentation simulation, neutron and x-ray diffraction analyses are contradictory in predicting both compressive[16] and tensile[18,19] hoop stresses at the indentation base. Indeed, in general, numerical studies of quasi-static indentation predict either tensile hoop stresses at the base[20] and rim[21] or compressive hoop stresses at the base[22] and rim[20] of the indentation sites; experimental studies, conversely, report only tensile hoop stresses at the rim.[23] Consequently, in the present work, we attempt to characterize the residual stress field of simulated FOD sites using preliminary x-ray micro-diffraction studies, numerical analysis by Hutchinson *et al.*[21] and the available literature. These analyses suggest zones of tensile residual hoop stresses located at the base and rim of the indentation sites, consistent with the location of the preferred sites for crack initiation.

D. *Microstructure*

Microstructural variability through thermomechanical treatment is known to have a marked influence on the fatigue properties of titanium alloys, as noted in several recent reviews.[24-26] Correspondingly, microstructural changes associated with FOD-induced plasticity must be taken into account in any assessment on the role of FOD. This is evident from shot peening studies on Ti-6Al-4V (e.g., Refs. 27,28) where, by separating the influence of microstructure from residual stress effects, it was observed that the deformed microstructure exhibited an increased resistance to crack nucleation, yet at the same time a drastically reduced resistance to small-crack growth.[29]

III. EXPERIMENTAL PROCEDURES

A. *Material*

The Ti-6Al-4V alloy under study was part of a set of forgings produced specifically for the U.S. Air Force sponsored programs on high cycle fatigue. Its chemical composition is given in Table I. The β-transus is at ~996°C. Mill annealed 63.5 mm diameter bar stock material, originating from Teledyne Titanium, was forged in one stroke at 938°C on a closed-end channel die to a plate size of 400×150×20 mm, followed by air-cooling. The forging plates were then solution treated in an air furnace at 927°C for 1 hr followed by fan air cooling; this resulted in a cooling rate of ~200°C/min. Finally, the plates were stress relieved *in vacuo* for 2 hr at 705°C. Further material and processing details are given in Ref. 30.

After such thermomechanical processing, the plate material showed a bimodal microstructure with a volume fraction of ~60% primary α (diameter ~20 μm) within a lamellar α+β matrix (Figure 1). This microstructure has been termed "solution treated and overaged" (STOA). The crystallographic texture of the plate material was measured using Ni-filtered Cu-K_α radiation, and is plotted as (0002) and $\{10\bar{1}0\}$ pole figures in Figure 2. In this figure, the numbers represent the ratio of the intensities of the (0002) basal and $\{10\bar{1}0\}$ prismatic planes of the hexagonal closed packed α phase to that of the random texture of the hot isostatic pressed powder standard. The resulting pole figures reveal preferred orientation of the basal planes parallel and perpendicular to the length of the forged plate (L-direction).

Uniaxial tensile properties (parallel to the length of the plate, L-orientation) are listed in Table II; the tensile tests were performed at an initial strain rate of 8×10^{-4} s^{-1}.

B. *Simulation of Foreign Object Damage*

In this study, foreign object damage by hard particles was simulated by shooting steel spheres onto a flat specimen surface to produce a single specific damage site. Chrome-hardened steel spheres, 3.2 mm in diameter with a Rockwell C hardness of 60, were impacted onto the flat surfaces of the tensile fatigue (so-called K_B) specimens at an angle of 90º (normal impact, Figure 3) at velocities of 200, 250 and 300 m/s using a compressed-gas gun facility. These velocities

represent typical in-service impact velocities on aircraft engine fan blades. The spheres were accelerated by applying gas pressures between 2 and 7 MPa; their velocity was measured photoelectrically prior to impact.

C. *Fatigue Test Methods*

1. *Smooth-bar and small-crack fatigue tests*

For an assessment of FOD on the fatigue behavior, baseline stress/life (S-N) fatigue data of the bimodal Ti-6Al-4V plate material were generated on smooth-bar hourglass specimens. Specimens were machined, with the geometry shown in Figure 4(a), such that the specimen axis was oriented parallel to the length of the plate (L-orientation). They were electrolytically polished to minimize the presence of surface residual stresses and high dislocation densities from the machining. A solution of 59% methanol, 35% 2-butanol and 6% perchloric acid was used at -30°C and 16 V to remove a surface layer of 100 μm. S-N tests were performed on a Roell Amsler resonant-fatigue-testing machine in room temperature air at a cyclic frequency of 85 Hz.

To investigate small-crack propagation behavior, ~45 to 60 μm surface cracks were naturally-initiated at a load ratio ($R = \sigma_{min}/\sigma_{max}$) of -1 and an alternating stress of 650 MPa. After initiation, the load ratio was changed to 0.1 and small-crack growth was monitored at a maximum stress of 550 MPa. Tests were periodically interrupted to measure the surface crack length, 2*c*, in a light microscope. The stress-intensity range, ΔK, of the small semi-elliptical surface cracks was calculated using the Newman-Raju linear-elastic relationship:[31]

$$\Delta K = \Delta\sigma\sqrt{\pi \frac{a}{Q}}\, F \qquad [1]$$

where $\Delta\sigma$ is the stress range, *a* is the crack depth, *F* is the stress-intensity boundary correction factor, and *Q* the crack shape correction factor. For the present alloy, a crack depth to surface crack length, *a*/2*c,* ratio of 0.45 was assumed, based on fractographic observations.

Fatigue limits were also investigated using the so-called HCF step test. Using modified K_B specimens, this test consisted of loading in steps of 10^8 cycles at 1000 Hz at a constant stress amplitude. If no failure occurred after 10^8 cycles, the maximum stress level was successively

increased ~50 MPa until specimen failure. This procedure permits an estimation of the HCF fatigue limit with a single specimen.

2. *Large-crack fatigue tests*

The corresponding crack-growth tests on large cracks, typically in excess of ~5 mm in length, were performed on compact-tension C(T) specimens in general accordance with ASTM standard E-647. The C(T) specimens were machined in the L-T orientation with an 8 mm thickness and 25 mm width. Tests were carried out in room temperature air at R-ratios varying from 0.1 to 0.95 under automated load or stress-intensity control at frequencies between 50 and 1000 Hz (sinusoidal wave form). Fatigue-crack growth thresholds, ΔK_{TH} and $K_{max,TH}$, defined at a propagation rate of 10^{-10} m/cycle at 50 Hz and 10^{-11} m/cycle at 1000 Hz, were determined at load ratios of R = 0.1 to 0.8 using constant R testing; loads were shed such that $\Delta K = \Delta K_{initial} \exp[C(a-a_{initial})]$, with the normalized K-gradient, C, set to $-0.08 mm^{-1}$ (a and $a_{initial}$ are the instantaneous and initial crack lengths, respectively). For load ratios above 0.8, thresholds were approached using variable-R, constant-K_{max}/increasing-K_{min} loading. All testing was performed on automated MTS servo-hydraulic testing machines; experiments at 1000 Hz were conducted with a newly developed system using a voice-coil servovalve (further details of this instrument are described in Ref. 32).

Back-face strain unloading compliance techniques were used for *in situ* crack length measurements; crack lengths were periodically verified with optical measurements. Unloading compliance was also used to assess crack closure loads. Specifically, the closure stress intensity, K_{cl}, was determined at first contact of the crack surfaces, measured at the point of first deviation from linearity in the elastic compliance curve upon unloading.[33]

3. *FOD specimen fatigue tests*

To investigate the influence of foreign object damage on the fatigue behavior of the bimodal Ti-6Al-4V, modified K_B specimens were chosen (Figure 4(b)). This specimen geometry, which is essentially identical to that used by GE Aircraft Engines for its similarity to the blade-loading

configuration, [34] was machined with a rectangular gauge section (3.2 mm × 5.2 mm) with cylindrical buttonhead grip sections. To provide a consistent, nominally stress-free surface, the gauge section was prepared using standard stress relief and chemical-milling procedures. To simulate FOD, steel shot was fired at 90° to the specimen surface at velocities of 200 to 300 m/s, as noted above. After impacting, specimens were cycled at 20 Hz (sinusoidal waveform) with a maximum stress of 500 MPa at a load ratio of R = 0.1. To detect fatigue crack initiation, specimens were removed periodically from the test frame and examined in a scanning electron microscope (SEM); once a crack had initiated, the same procedure was used to monitor subsequent small crack growth. Stress intensities for the surface cracks were again calculated from Eq. [1] assuming a crack depth to surface crack length ratio, $a/2c$, of 0.45 (determined from fractographic observations).

As an initial assessment of the stress concentration associated with the damage sites, elastic stress-concentration factors, k_t, surrounding the indentations were determined based on three-dimensional photoelastic experiments performed by Nisida *et al.*[35] Figure 5 shows schematically the stress distribution surrounding a 300 m/s impact indentation site. Table III lists the impact site geometry dimensions and the resulting elastic stress-concentration factors, which reach a maximum at the base of the indents, i.e., ranging from k_t = 1.6 (for a 300 m/s impact site) to k_t = 1.4 (for a 200 m/s site). Corresponding values at the crater surface rim range from k_t = 1.25 (300 m/s) to k_t = 1.15 (200 m/s).

To compute local stress-intensity factors for small cracks emanating from such indentations, incorporating both indentation geometry and stress concentration effects, the relationship of Lukáš [36] for small cracks at notches is used, viz:

$$\Delta K = \frac{1.244 k_t}{\sqrt{1 + 4.5(a/\rho)}} \Delta\sigma\sqrt{\pi a} \qquad [2]$$

where $\Delta\sigma$ is the stress range, a is the crack depth, and ρ is the indentation radius. However, it should be noted that the contribution to this value from the residual stress field surrounding the indentation has not been taken into account, due to uncertainty in the value of these local stresses.

Current studies are focused on the use of synchrotron x-ray micro-diffraction methods, together with numerical analysis,[21] to estimate these local stress gradients.

IV. RESULTS AND DISCUSSION

A. *Characterization of Foreign Object Damage*

The simulated foreign object damage sites are characterized in terms of size, shape and possible occurrence of microcracking in Figures 6, 7 and 8 (and Table III), and with respect to induced microstructural changes in Figure 9. Damage clearly can be seen to be a function of impact velocity. Based on these observations, the distribution of the residual stresses surrounding the impact site was deduced, as discussed below, and is shown schematically in Figure 10.

First with respect to shape, Figure 6 shows a schematic of the cross section of a crater formed by a normal impact. The measured dependence of the crater diameter, W, and depth, δ, on the impact velocity are listed in Table III. SEM micrographs show indentations formed at impact velocities of 200 m/s (Figure 7(a)) and 300 m/s (Figure 7(b)). At velocities above 250 m/s, a pronounced pile-up at the crater rim, with some detached material (Figure 7(b)), was evident. Of critical importance were the observations, shown in Figure 8, that for the highest velocity impacts at 300 m/s, plastic flow of material at the crater rim causes local notches (Figure 8(a)) and even microcracking (Figure 8(b)). The microcracks were quite small, i.e., between ~2 to 10 μm in depth, but clearly provided the nucleation sites for subsequent HCF cracking, as shown in Figure 8(c). No such microcracking could be detected in this alloy at lower impact velocities.

The resulting deformed microstructures, imaged at the center, mid and rim position of the crater (Figure 9), reveal flattened primary α grains at the base of the indent (Figure 9(b)), whereas at the mid (Figure 9(c)) and rim locations (Figure 9(d)), the α grains are deformed in shear, along with the lamellar matrix of the bimodal microstructure. Bulk plastic deformation of the material surrounding the impact crater was found to extend into a region of approximately one indentation radius. At the base of the impact crater, strongly localized deformation can be seen in form of circumferentially-oriented intense shear bands emanating from the surface of the

impact crater (see arrows in Figures 9(c) and 9(d)). The work of Hutchings and Timothy[37-40] showed that such shear bands form adiabatically during impact in Ti-6Al-4V. For that reason, it is anticipated that localized plasticity due to adiabatic heating is the reason for the pronounced pile-up formation at crater rim. This is consistent with the observation that intense shear banding and pile-ups at the crater rim were only observed for 250 and 300 m/s impacts; neither feature was evident for 200 m/s velocities. This result is consistent with the reported critical velocity of 214 ± 16 m/s for shear banding in bimodal Ti-6Al-4V with 3.2 mm diameter steel sphere impacts.[40]

Contrary to the shot peening process, where the surface deformation from multiple impacts imparts compressive residual stresses at the component surface,[27,28] with the single impacts typical of FOD, zones of both tensile and compressive residual stresses appear to be generated in the vicinity of the impact site. A proposed residual stress distribution is shown schematically in Figure 10. Upon impact, the stress state in the target material directly beneath the indenter is subjected to a compressive radial stresses, σ_r, and tensile hoop stresses, σ_θ. This is illustrated in Figure 10(a) together with the region of bulk plastic deformation, pile-up formation at the impact site rim, circumferential oriented adiabatic shear bands and area of localized hydrostatic pressure at the indent base. The corresponding state of residual stresses after unloading is shown in Figure 10(b). The overall constraint of the surrounding elastic material leads to compressive residual hoop stresses, σ_θ, and tensile residual radial stresses, σ_r, in the bulk of the plastically deformed material beneath the indentation crater. In addition, three distinct areas of tensile residual hoop stress are generated, namely (i) surrounding the bulk compressive residual stress zone, due to the balance of tensile and compressive stresses as in shot-peened components,[27] (ii) at the crater rim, due to geometrical constraint, and (iii) in a shallow surface layer at the base of the indent, due to hydrostatic compressive stresses from contact between indenter and the target material in this location. As such hydrostatic pressure reduces the magnitude of shear stresses, intense shear bands were only found in regions away from the base of the indent (Figure 9(a)).

B. *Baseline Fatigue Properties*

1. *Fatigue crack initiation*

To define baseline conditions, the smooth-bar S-N fatigue properties of the bimodal Ti-6Al-4V material, from tests on unnotched, electrolytically-polished hourglass specimens, are shown in Figure 11.[41] These data indicate the dependence of the maximum stresses (σ_{max}) at three different load ratios (R = -1, 0.1, 0.5) on the number of cycles to failure, N_F, and show that increasing the load ratio leads to an increase in σ_{max} at the 10^7-cycle fatigue limit from 375 MPa (R = -1) to 500 MPa (R = 0.1) and 625 MPa (R = 0.5).

Small surface cracks, ~45-60 μm in size, were observed to nucleate after roughly 10,000 cycles at σ_{max} = 650 MPa at R = -1 (Figure 12). Microstructurally, cracks tended to initiate in planar slip bands within the globular α-phase, specifically at the surface at R = -1 (Figure 12) and subsurface at R = 0.1 and 0.5 (Figure 13). Final failure occurred at a maximum stress of 475 MPa (R = 0.1) after ~5.3×10^7 cycles.

As noted above, the current "safe-life" design approach against HCF failure is based on fatigue limit data generated through S-N tests. To incorporate the influence of load ratio, modified Goodman diagrams were constructed where the limiting alternating stress is plotted against the mean stress for, i.e., the 10^7-cycle fatigue limit. Figure 14 shows such a Goodman diagram[42] constructed from the 10^7-cycle fatigue limit fatigue data for bimodal Ti-6Al-4V presented in Figure 11. It can be seen as the mean stress becomes more tensile, the allowable stress amplitude is reduced, and can be plotted as a nearly linear decrease from the fatigue limit at R = -1 to the tensile strength (σ_a = 0).

2. *Fatigue-crack growth of small and large cracks*

For the alternative damage-tolerant design approach against HCF, baseline data of near-threshold fatigue-crack growth rates and fatigue thresholds (ΔK_{TH}) are required, ideally for both naturally-initiated small cracks and through-thickness large cracks.

Smooth-bar hourglass specimens were pre-cracked at a load ratio of R = -1 (to avoid subsurface initiation at positive R ratios); 10,000 cycles at a stress amplitude of 650 MPa resulted

in ~10 to 15 surface cracks with surface lengths ranging from ~45 to 60 μm. Subsequent crack-growth behavior of the naturally-initiated small cracks was then monitored optically at a maximum stress of 550 MPa at R = 0.1, i.e., 50 MPa above the 10^7-cycle fatigue limit.[41] The resulting growth rates as a function of the applied stress-intensity range are shown in Figure 15, and are compared with corresponding large crack results based on compact-tension testing. Characteristic of the small-crack effect,[43-45] the growth rates of the small cracks were up to one order of magnitude higher than those of equivalent large cracks at the same applied stress-intensity range.

Since the majority of the small cracks have dimensions larger then the characteristic size-scales of the microstructure, it is reasoned that one of the prime reasons for the small-crack effect is the reduced role of crack-tip shielding (e.g., surface roughness induced crack closure) due to their limited crack wake (e.g., Ref. 46). Based on this consideration, two types of large-crack tests were performed to minimize the extent of closure in order to simulate the small-crack results on conventional C(T)-specimens.[47] Specifically, this involved load shedding to approach the threshold using (i) constant-R testing at high load ratios (R ~ 0.8), and (ii) constant-K_{max}/increasing-K_{min} testing, both procedures that tend to minimize crack wedging by ensuring that the crack-tip opening displacements (CTODs) are large enough to limit any premature contact of the crack surfaces upon unloading, i.e., the minimum CTOD in the loading cycle is larger than the dimension of the fracture surface roughness. Results are compared with the naturally-initiated small-crack data in Figure 15.

Although the growth rates of the small cracks still exceed those of the "closure-free" large-cracks, the thresholds determined using the constant-K_{max}/increasing-K_{min} large-crack tests appear to provide a worst-case for both large and small crack results. As discussed elsewhere,[9] the threshold value of ΔK_{TH} = 1.9 MPa√m (at 4×10^{-12} m/cycle) at a maximum load ratio of R = 0.95 (above which $K_{max} > K_{Ic}$), is lower than the stress-intensity range required for the growth of naturally-initiated small cracks (~2.9 MPa√m), and as such is considered as a *practical* lower-bound threshold for this alloy.

Further verification of this "worst case" threshold concept was afforded by smooth-bar experiments, where specimens were naturally pre-cracked at R = -1 (stress amplitude of 650 MPa) to different initial surface crack lengths. The stress amplitude was then changed to give a ΔK of 1.5 MPa$\sqrt{m}$ (at R = -1 and 0.5) and the specimens cycled for ~4 to 5×10^7 cycles. The test conditions are listed in Table IV. In all cases, no crack growth was detected at ΔK = 1.5 MPa$\sqrt{m}$.

The higher growth rates of the naturally-initiated small-cracks, compared to the "closure-free" large cracks, are presumed to be associated with biased statistical sampling of the microstructure. The natural crack initiation process allows for sampling of a very large area of the specimen for more favorable microstructural orientations with respect to crack initiation and growth, compared to that of the large cracks which essentially sample an average of all microstructural orientations.

C. *Effect of Foreign Object Damage*

The overall effect of FOD, simulated by impacting fatigue test specimens with high-velocity steel shot, was to markedly reduce the fatigue life compared to that obtained with undamaged smooth-bar specimens (Figure 16). At a nominal (far-field) maximum stress of 500 MPa (R = 0.1), small surface cracks (c ~ 50 μm) were initiated at the FOD impact sites within ~3 to 5×10^4 cycles, with final failure occurring between ~4 to 8×10^4 cycles. These results show that the fatigue lives were drastically reduced by over two orders of magnitude by FOD, compared to the undamaged smooth-bar properties.

As discussed above, the reduction in fatigue strength due to FOD can be considered principally in terms of earlier crack initiation due to four salient factors:

- *stress concentration:* FOD creates stress-raising notches; their geometry influences the local stress fields in the vicinity of the impact sites
- *FOD-initiated microcracking*: at the highest impact velocities (and in brittle alloys[14]), microcracks may be formed in the damage zone, and provide a potent site for the initiation of HCF cracking
- *residual stresses:* FOD induces a residual stress state, both tensile and compressive,

surrounding the impact site due to plastic deformation associated with the impact

- *microstructure:* FOD changes the nature of the microstructure at the damage site, again due to plastic deformation associated with the impact.

1. *Fatigue crack initiation*

Examples of initiation sites of small surface cracks are shown in Figure 17(a) for a 250 m/s impact and in Figure 17(b) for a 300 m/s impact. First results show that the cracks tended to initiate at the bottom of the indent for the lower velocity impacts (200 and 250 m/s) and at the crater rim for the higher velocity impacts (300 m/s). The position of the crack front during crack extension, both depthwise and on the surface, is indicated in these micrographs; this was determined from surface crack length measurements during the test and subsequent fractography (as the local crack front is oriented perpendicular to the "river markings").

For the 200 and 250 m/s impacts, fatigue crack initiation can be seen on the surface at the base of the indent (Figure 18), and is explained by the stress concentration from the notch geometry. For these impact conditions, the notches are relatively shallow with k_f values of ~1.4, close to the corresponding elastic stress-concentration factors of $k_t \sim 1.4$ to 1.5 (Table III).

For the 300 m/s impacts, initiation conversely occurred at the crater rim. Indeed, impact studies by Gros *et al*.[16] also report fatigue crack initiation both at the base and rim of high-velocity impacts in medium-carbon steel. Similarly, Ruschau *et al*.[17] observe crack initiation at the rim location for 60° impact angles (glass beads) on simulated fan blade leading-edge specimens of Ti-6Al-4V. For crack initiation at the rim, stress concentration due to gross indentation geometry is clearly not the only effect as the location of the maximum stress-concentration factors is still at the base ($k_t \sim 1.6$ and $k_f \sim 1.54$ at the base, compared to a value of $k_t \sim 1.25$ at the crater rim). Here, the tensile residual stresses and highly deformed microstructure play an additional role. The tensile hoop stresses are critical as they superimpose onto the nominally applied stresses resulting in higher maximum and mean stresses, and in turn earlier crack initiation and faster crack-growth rates. However, more importantly, at these high impact velocities, small microcracks were detected in the vicinity of the crater rim (Figure 8(b)), and

clearly provide the preferred site for fatigue-induced crack propagation (Figure 8(c)). The fact that such microcracks only develop in this alloy at the highest impact velocities strongly implies that the simulation of FOD using lower velocity impacts will not necessarily involve all the damage processes associated with the phenomenon.

The presence of adiabatic shear bands does not appear to play a significant role in the initiation process of the fatigue cracks. This is thought to be due to the fact that at the prime locations for crack initiation, i.e., at the base of the indent for the 200 to 250 m/s impacts and at the crater rim for 300 m/s impacts, the tangential aligned shear bands are oriented parallel to the applied stress axis.

2. *Fatigue crack propagation*

The growth rates of the small cracks emanating from the 200 to 300 m/s impact sites are compared as a function of the stress-intensity range (ignoring stress concentration and residual stress effects, open symbols) in Figure 19 with the baseline growth-rate data for large (>5 mm) and naturally-initiated small (~45 to 1000 μm) cracks; also shown are the surface crack lengths, $2c$, of the small cracks. It can be seen that both the naturally-initiated and FOD-initiated small-crack growth rates are within the same scatter band and are roughly an order of magnitude faster than corresponding large-crack results. Furthermore, it can be seen, that the small-crack data tends to merge with large-crack results as the crack size increase, specifically above ΔK = 10 MPa√m. With respect to the fatigue-crack growth thresholds, however, in the data collected to date, no FOD-initiated cracks have been observed in the studies on Ti-6Al-4V with a bimodal microstructure below a stress-intensity range of ΔK = 2.9 MPa√m, which is over 50% higher than the worse-case (large-crack) threshold of 1.9 MPa√m. Consequently, we conclude that fatigue-crack propagation thresholds for large cracks, determined under conditions that minimize crack closure, can be used as a practical lower bound for the threshold stress intensities for naturally-initiated and FOD-initiated small cracks in this alloy.

Also shown in Figure 19 are the results of the initial assessment to correct for the effect of stress concentration on the calculation of stress intensities, and hence the crack-growth rates, of

the FOD initiated small cracks using the Lukáš[36] solution (Eq. [2]) (closed symbols). The overall effect is that the correction yields a closer correspondence between data from high load-ratio large-cracks and FOD-initiated small-cracks.

However, at crack sizes above $2c \sim 100$ μm, the crack-growth rates of the FOD-initiated small cracks are distinctly slower than that of the naturally-initiated small cracks. Although this effect may be associated with experimental uncertainty, it is reasoned that the effect most probably results from the presence of compressive residual hoop stresses throughout the impact-damaged zone. This implies that whereas FOD may promote crack initiation and early small-crack growth due to the tensile residual stresses and (at high impact velocities) microcracking local to the surface at the base and rim of the indent, subsequent crack growth may indeed be retarded compared to naturally-initiated cracks, due to the presence of the compressive residual stresses.

There is an additional influence of FOD from the presence of the impact-damaged microstructure, which can be seen by comparing the growth mechanisms of small cracks in smooth-bar (Figure 13) and FOD (Figure 18) specimens. In smooth-bar specimens, naturally-initiated small cracks propagate predominantly in slip bands within the primary α phase; this is attributed to the planar-slip distribution and the relatively large slip length associated with the inherent crystallographic texture (Figure 2) and high volume fraction of primary α.[48] In impacted samples, conversely, the slip distribution is more homogeneous such that this planar slip-band cracking mechanism is not seen, presumably because the FOD-induced plastic deformation breaks up easy crack paths along single slip bands. This effect of a change in the planarity of slip on the small-crack growth behavior in impact-damaged microstructures is currently under examination as it is known from studies[49,50] on high-strength aluminum alloys that crack propagation involving inhomogeneous planar (single) slip is much faster than crack propagation involving homogeneous (multiple) slip ahead of the crack tip.

V. SUMMARY AND CONCLUSIONS

An increasing proportion of high-cycle fatigue related failures of military gas-turbine engines has inspired a recent re-examination of the design methodologies for HCF-critical components. In view of the in-service conditions, i.e., small crack sizes, high mean loads and high frequency (>1 kHz) vibratory loading, damage-tolerant design methodologies based on the concept of a threshold for no fatigue-crack growth would appear to offer the best approach. As foreign object damage has been identified as one of the prime sources of HCF-related failures, the current study has focused on the role of (simulated) foreign object damage in influencing fatigue-crack growth thresholds and early crack growth of both large and small cracks in an aero-engine fan blade titanium alloy, Ti-6Al-4V, processed with a bimodal microstructure. Based on this work, the following conclusions can be made:

1. FOD, simulated by the high-velocity (200 to 300 m/s) impacts of steel spheres on a flat surface, results in a significant loss in resistance to HCF. At the smooth-bar 10^7-cycle fatigue limit, for example, crack initiation lives of FOD-samples were less than 4×10^4 cycles, three orders of magnitude lower than lifetimes for undamaged samples.
2. The primary role of FOD is to provide preferred sites for the premature initiation of fatigue cracks. For 200 to 250 m/s impacts on bimodal Ti-6Al-4V, such cracking initiated at the base of the indentations, whereas at 300 m/s, initiation occurred at the crater rim.
3. The detrimental effect of FOD results from (i) the stress concentration associated with the FOD indentation, (ii) the presence of small microcracks at the crater rim of the damaged zone (seen only at the highest impact velocities), (iii) the localized presence of tensile residual hoop stresses at the base and rim of the indent sites, and (iv) microstructural damage from FOD-induced plastic deformation.
4. The subsequent propagation of small cracks within the damage zone, however, is somewhat slower than the corresponding propagation rates of naturally-initiated small cracks at the same applied stress-intensity levels. This appears to be associated with two effects, namely (i) the presence of compressive residual stresses throughout most of the damaged zone, and

(ii) the fact that FOD-induced plastic deformation tends to suppress planar slip-band cracking by making the slip distribution more homogeneous.

5. No crack growth from the FOD impact (or natural-initiation) sites has been observed to date at ΔK values below ~2.9 MPa√m. This is over 50% higher than the "closure-free", *worse-case* threshold value of ΔK_{TH} = 1.9 MPa√m, defined for large cracks in bimodal Ti-6Al-4V at the highest possible load ratio. The worst-case, large-crack threshold can thus be used as a practical lower-bound to FOD-initiated cracking in this alloy.

ACKNOWLEDGEMENTS

This work was supported by the Air Force Office of Scientific Research, Grant No. F49620-96-1-0478, under the auspices of the Multidisciplinary University Research Initiative on *High Cycle Fatigue* to the University of California, Berkeley. We acknowledge additional support from the Hertz Foundation for B.L.B. in the form of a graduate fellowship. Tensile test, texture measurements and smooth-bar testing were conducted at Technical University of Hamburg-Harburg, Germany, by J.O.P. in collaboration with Dr. J. A. Hines and Prof. G. Lütjering. Special thanks are due to Prof. Werner Goldsmith (UCB) for providing the compressed-gas gun facility, and to Prof. J. W. Hutchinson, J. P. Campbell and Dr. J. M. McNaney for helpful discussions.

REFERENCES

1. B.A. Cowles: *Int. J. Fract.*, 1996, vol. 80, pp. 147-63.
2. T. Nicholas and J.R. Zuiker: *Int. J. Fract.*, 1996, vol. 80, pp. 219-35.
3. J.M. Larsen, B.D. Worth, C.G. Annis, Jr., and F.K. Haake: *Int. J. Fract.*, 1996, vol. 80, pp. 237-55.
4. R.O. Ritchie: in *Proc. ASME Aerospace Division*, J.C.I. Chang, J. Coulter, D. Brei, W.H.G. Martinez, and P.P. Friedmann, eds., 1996, AD-Vol. 52, ASME, pp. 321-33.
5. *Erosion, Corrosion and Foreign Object Damage Effects in Gas Turbines*, AGARD Conference Proceedings No. 558, North Atlantic Treaty Organization. Advisory Group for Aerospace Research and Development, Propulsion and Energetics Panel, 1994
6. T. Nicholas, J.P. Barber, and R.S. Bertke: *Experimental Mechanics*, October 1980, pp. 357-64.
7. S.J. Hudak, Jr., G.G. Chell, T.S. Rennick, R.C. McClung, and D.L. Davidson: in *Proceedings of 4th National Turbine Engine HCF Conference, CD Rom, Session 10, Materials Damage Tolerance IV*, 1999, pp. 7-17.
8. P. Gravett, R. Bellows, T. Dunyak, D. Herrmann, and S. Hudak, Jr.: in *Proceedings of 4th National Turbine Engine HCF Conference, CD Rom, Session 10, Materials Damage Tolerance IV*, 1999, pp. 1-6.
9. O. Roder, J.O. Peters, B.L. Boyce, A.W. Thompson, and R.O. Ritchie: in *Proceedings of 4th National Turbine Engine HCF Conference, CD Rom, Session 10, Materials Damage Tolerance IV*, 1999, pp. 41-50.
10. R.O. Ritchie, D.L. Davidson, B.L. Boyce, J.P. Campbell, and O. Roder: *Fat. Fract. Eng. Mat. Struct.*, 1999, in press.
11. N.E. Frost: *Proc. Instn. Mech. Engrs.*, 1959, vol. 173, pp. 811-827.
12. N.E. Dowling: *Fat. Eng. Mat. Struct.*, 1979, vol. 2, pp. 129-39.
13. M.H. El Haddad, T.H. Topper, and K.N. Smith: *Eng. Fract. Mech.*, 1979, vol. 11, pp. 573-84.

14. T.S. Harding, J.W. Jones, P.S. Steiff, and T.M. Pollock: *Scripta Mater.*, 1999, vol. 40, pp. 445-49.

15. J.L. Hamrick, II, S. Mall, and T. Nicholas: in *Proceedings of 4th National Turbine Engine HCF Conference, CD Rom, Session 8, Materials Damage Tolerance IV*, 1999, pp. 38-48.

16. V. Gros, B. A. Taweel, M. Ceretti, C. Prioul, and A. Lodini: in *Proc. 4th European Conf. on Residual Stresses*, S. Denis, J.-L. Lebrun, B. Bourniquel, M. Barral, and J.-F. Flavenot, eds., SF2M, ENSAM, 1996, pp. 567-75.

17. J.J. Ruschau, S.R. Thompson, J.J. Kleck, and T. Nicholas: in *Proceedings of 4th National Turbine Engine HCF Conference, CD Rom, Session 8, Materials Damage Tolerance IV*, 1999, pp. 28-37.

18. K.-P. Hornauer, H.H. Jühe, A. Klinkenberg, and P. Starker: *Härtereitechnische Mitteilungen*, 1981, vol. 36, pp. 322-26.

19. M. Kobayashi, T. Matsui, and Y. Murakami: *Int. J. Fatigue*, 1998, vol. 20, pp. 351-57.

20. G.B. Sinclair, P.S. Follansbee, and K.L. Johnson: *Int. J. Solids Struct.*, 1985, vol. 21, pp. 865-88.

21. J.W. Hutchinson: Harvard University, private communication, 1999.

22. C. Hardy, C.N. Baronet, and G.V. Tordion: *Int. J. Numer. Meth. Engin.,* 1971, vol. 3, pp. 451-62.

23. C.J. Studman and J.E. Field: *J. Mater. Sci.*, 1977, vol. 12, pp.215-18.

24. G. Lütjering: *Mater. Sci. Eng.*, 1998, vol. A243, pp. 32-45.

25. A.W. Thompson: in *Fatigue Behavior of Titanium Alloys*, R.R. Boyer, D. Eylon, J.P. Gallagher, and G. Lütjering, eds., TMS, Warrendale, PA, 1999, in press.

26. W.J. Evans: *Mater. Sci. Eng.*, 1999, vol. A263, pp. 160-75.

27. L. Wagner and G. Lütjering: in *Proc. 2nd Int. Conf. Shot Peening*, H.O. Fuchs, ed., American Shot Peening Society, Paramus, NJ, 1984, pp.194-200.

28. L. Wagner and G. Lütjering: in *Proc. 2nd Int. Conf. Shot Peening*, H.O. Fuchs, ed., American Shot Peening Society, Paramus, NJ, 1984, pp.201-7.

29. H. Gray, L. Wagner, and G. Lütjering: in *Shot Peening*, H. Wohlfahrt, R. Kopp, and O. Vöhringer, eds., DGM, 1987, pp. 467.
30. D. Eylon: Summary of the Available Information on the Processing of the Ti-6Al-4V HCF/LCF Program Plates, University of Dayton Report, Dayton, OH, 1998.
31. J.C. Newman, Jr., and I.S. Raju: *Eng. Fract. Mech.*, 1981, vol. 15, pp. 185-92.
32. J.M. Morgan and W.W. Milligan: in *High Cycle Fatigue of Structural Materials*, W.O. Soboyejo, and T.S. Srivatsan, eds., TMS, Warrendale, PA, 1997, pp. 305-12.
33. R.O. Ritchie and W. Yu: in *Small Fatigue Cracks*, R.O. Ritchie and J. Lankford, eds., TMS, Warrendale, PA, 1986, pp. 167-89.
34. A. Coles, R.E. Johnson, and H.G. Popp: *J. Eng. Mater. Technol.*, 1976, pp. 305-15.
35. M. Nisida and P. Kim: in *Proc. 12th Nat. Cong. Applied Mechanics*, 1962, pp. 69-74.
36. P. Lukáš: *Eng. Fract. Mech.*, 1987, vol. 26, pp. 471-73.
37. I.M. Hutchings: in *Materials Behavior under High Stress and Ultra High Loading Rates,* J. Mescall and V. Weiss, eds., Plenum Press, NY, 1983, pp. 161-96.
38. S.P. Timothy and I.M. Hutchings: *Acta Metall.*, 1985, vol. 33, pp. 667-76.
39. S.P. Timothy and I.M. Hutchings: *Eng. Fract. Mech.*, 1984, vol. 7, pp. 223-27.
40. S. P. Timothy and I. M. Hutchings: in *Proc. of the 3rd Conf. on the Mechanical Properties of Materials at High Rates of Strain*, The Institute of Physics, Bristol and London, UK, 1984, pp. 397-404.
41. J.A. Hines, J.O. Peters, and G. Lütjering: in *Fatigue Behavior of Titanium Alloys*, R.R. Boyer, D. Eyla, J.P. Gallagher, G. Lütjering, eds., TMS, Warrendale, PA, 1999, in press.
42. J. Goodman: *Mechanics Applied to Engineering*, Longmans, Green & Co., Ltd., London, UK, 1899.
43. R.O. Ritchie and J. Lankford, eds.: *Small Fatigue Cracks*, TMS-AIME, Warrendale, PA, 1986.
44. K.J. Miller and E.R. de los Rios, eds.: *The Behaviour of Short Fatigue Cracks*, The Mechanical Engineering Publishing Ltd., London, UK, 1986.

45. K.J. Miller and E.R. de los Rios, eds.: *Short Fatigue Cracks*, The Mechanical Engineering Publishing Ltd., London, UK, 1992.
46. R.O. Ritchie and J. Lankford: *Mater. Sci. Eng.*, 1986, vol. 84, pp. 11-16.
47. B.L. Boyce, J.P. Campbell, O. Roder, A. W. Thompson, W. W. Milligan, and R. O. Ritchie: *Int. J. Fatigue*, 1999, in press.
48. J.A. Hines, J.O. Peters, and G. Lütjering: in *Fatigue Behavior of Titanium Alloys*, R.R. Boyer, D. Eylon, J.P. Gallagher and G. Lütjering, eds., TMS, Warrendale, PA, 1999, in press.
49. J.O. Peters, A. Gysler, and G. Lütjering: in *Proc. of ICAA-6, Aluminum Alloys*, 1998, vol. 3, pp. 1427-32.
50. J.O. Peters, A. Gysler, and G. Lütjering: in *Proc. of Fatigue '99 – 7th Int. Fatigue Conference*, X.-R. Wu and Z.-G. Wang, eds., 1999, EMAS Ltd., UK, pp. 1009-14.

LIST OF TABLES

Table I: Chemical composition of Ti-6Al-4V bar stock material in wt.-% [30]

Ti	Al	V	Fe	O	N	H
bal.	6.30	4.19	0.19	0.19	0.013	0.0041

Table II: Uniaxial tensile properties of bimodal Ti-6Al-4V

E: young's modulus, $\sigma_{0.2}$: yield stress, UTS: ultimate tensile strength, σ_F: true fracture stress, Tens. El.: tensile elongation, RA: reduction of area at fracture; strain rate 8×10^{-4} s^{-1}

E (GPa)	$\sigma_{0.2}$ (MPa)	UTS (MPa)	σ_F (MPa)	Tens. El. (%)	RA (%)
110	915	965	1310	19	45

Table III: Dimensions of impact craters and stress concentration factors

$\varnothing W$: chord width of impact crater, δ: indentation depth (see Figure 6), k_t, elastic stress concentration factor (after Nisida *et al.*[35]), k_f, effective-fatigue stress concentration factor

Impact Velocity	$\varnothing W$ (mm)	δ (mm)	k_t base	k_t rim	k_f
300 m/s	2.67	0.67	1.60	1.25	1.54
250 m/s	2.38	0.54	1.50	1.20	1.40
200 m/s	2.14	0.43	1.40	1.15	1.40

Table IV: Small-crack HCF-threshold of ΔK = 1.5 MPa$\sqrt{m}$ test

(Pre-cracking: 650 MPa, R = -1, N = 10,000 – 15,000 cycles); σ_a: stress amplitude, σ_m: mean stress, σ_{max}: maximum stress

Load ratio (R)	Initial surface crack length, $2c$ (μm)	σ_a (MPa)	σ_m (MPa)	σ_{max} (MPa)	ΔN (cycles)
R = -1 (ΔK based on tensile range)	110	170	0	170	$> 5 \times 10^7$
R = 0.5	65	112.5	337.5	450	$> 4 \times 10^7$
	90	93.75	281.25	375	$> 4 \times 10^7$
	230	60	180	240	$> 4 \times 10^7$

LIST OF FIGURE CAPTIONS

Fig. 1: Optical micrograph of the bimodal (STOA) microstructure of forged Ti-6Al-4V plate material (etched in 3½% HNO_3 - 5% HCl)

Fig. 2: Crystallographic texture of the forged Ti-6Al-4V shown as pole figures. Numbers represent the ratio of the intensities of the (a) (0002) basal and (b) $\{10\bar{1}0\}$ prismatic planes of the hexagonal closed packed α phase to that of the random texture of the hot isostatic pressed powder standard.

Fig. 3: Schematic illustration showing impact angles with respect to specimen geometry and loading axis for fatigue tests. In this study, a normal (90°) impact angle was chosen.

Fig. 4: Drawings of the specimen geometries used, showing (a) smooth-bar specimen for S-N curves, and (b) modified K_B specimen for simulated FOD studies. All dimensions are in mm.

Fig. 5: Schematic illustration showing the stress concentration surrounding a FOD indentation crater (based on Nisida *et al.*[35]).

Fig. 6: Schematic illustration of the cross section of simulated FOD crater after impact. (W is the chord width, δ is the depth).

Fig. 7: Scanning electron micrographs of impact damage sites for (a) 200 m/s and (b) 300 m/s impact velocities, indicating increasing damage with increasing velocity with respect to indentation size, lip formation at crater rim and intense shear band formation emanating at the indent surface.

Fig. 8: Scanning electron micrographs showing the presence of microcracking at crater rim of a FOD indent after the highest velocity (300 m/s) impacts. Micrographs show (a) local notches at crater rim caused by plastic flow of material, (b) microcracks emanating from such notches, and c) subsequent fatigue-crack growth initiated at such microcracks after 5000 cycles at σ_{max} = 500 MPa (R = 0.1).

Fig. 9: FOD following 300 m/s impacts, showing (a) schematic of the crater, and optical micrographs of cross sections at (b) the base (c) mid location, and (d) rim of the crater.

Note formation of shear bands emanating from the surface at mid and rim positions (marked by arrows).

Fig. 10: Model of high-velocity impact loading and resulting residual stress state, showing (a) state of stress at impact loading, and (b) state of residual stresses after impact loading (σ_r = radial stress, σ_θ = hoop stress).

Fig. 11: Stress-life (S-N) curves for bimodal Ti-6Al-4V, determined using smooth-bar specimens.[41] Also shown is the result of HCF step test at $R = 0.1$, based on modified K_B specimen testing.

Fig. 12: Optical micrograph showing surface crack initiation within globular α phase (R = -1, σ_{max} = 650 MPa, $N_F = 1 \times 10^4$ cycles).[41]

Fig. 13: Scanning electron micrograph showing subsurface crack initiation (see arrow) on a fatigue fracture surface of a modified K_B specimen (HCF step test at $R = 0.1$, σ_{max} = 475 MPa, $N_F = 5.3 \times 10^7$ cycles).

Fig. 14: Modified Goodman diagram showing the mean and alternating stress to give a life of $N_F = 1 \times 10^7$ cycles in bimodal Ti-6Al-4V, based on smooth-bar specimen tests (closed symbols). Also shown are data for the small-crack HCF threshold testing at $\Delta K = 1.5$ MPa$\sqrt{m}$ tests (open symbols).

Fig. 15: Variation in crack-growth rates, da/dN, with the applied stress-intensity range, ΔK, for naturally-initiated small cracks (~45 to 1000 μm)[41] and through-thickness large cracks (>5 mm) in bimodal Ti-6Al-4V. Small-cracks were initiated at σ_{max} = 650 MPa (R = -1). Large-crack growth data for $R \leq 0.8$ were derived from constant load-ratio tests, whereas for $R \geq 0.8$, constant-K_{max}/ increasing-K_{min} testing was used.

Fig. 16: The effect of FOD on the S-N data for bimodal Ti-6Al-4V, showing sharply reduced lifetimes. In addition, result of HCF step test at $R = 0.1$ is shown for smooth modified K_B specimen

Fig. 17: Scanning electron micrographs showing the growth of fatigue cracks initiated at FOD impact sites. The progressive position of the crack front is marked on the fracture

surface to indicate the initiation sites and crack shapes during crack extension for (a) 250 m/s impact, and (b) 300 m/s impact.

Fig. 18: Scanning electron micrograph of the fracture surface following fatigue of a 250 m/s FOD impacted K_B specimen, showing surface crack initiation (marked by the arrow) at the base of the indent (σ_{max} = 500 MPa, R = 0.1, $N_F = 7.9 \times 10^4$ cycles).

Fig. 19: Comparison of the variation in crack-growth rates, da/dN, with the applied stress-intensity range, ΔK, for FOD-initiated small cracks (~45 to 1000 μm) with that for naturally-initiated small cracks[41] and through-thickness large cracks in bimodal Ti-6Al-4V. Stress intensity data for FOD initiated crack growth has been corrected for the stress concentration associated with the indent using the K solution of Lukáš[36] and stress-concentration factors from Nisida *et al.*[35] (closed symbols); non-corrected data are shown for comparison (open symbols).

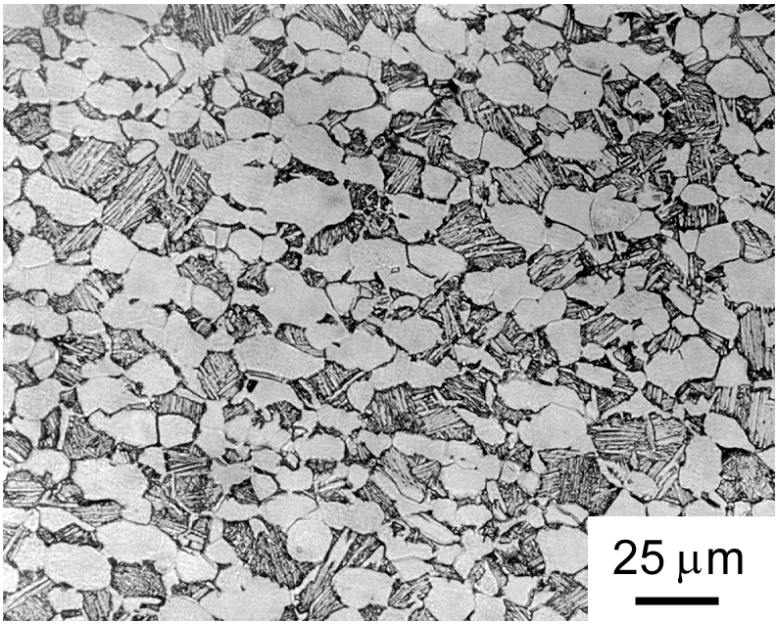

Fig. 1 - Optical micrograph of the bimodal (STOA) microstructure of forged Ti-6Al-4V plate material (etched in $3^1/_2$% HNO_3-5%HCl).

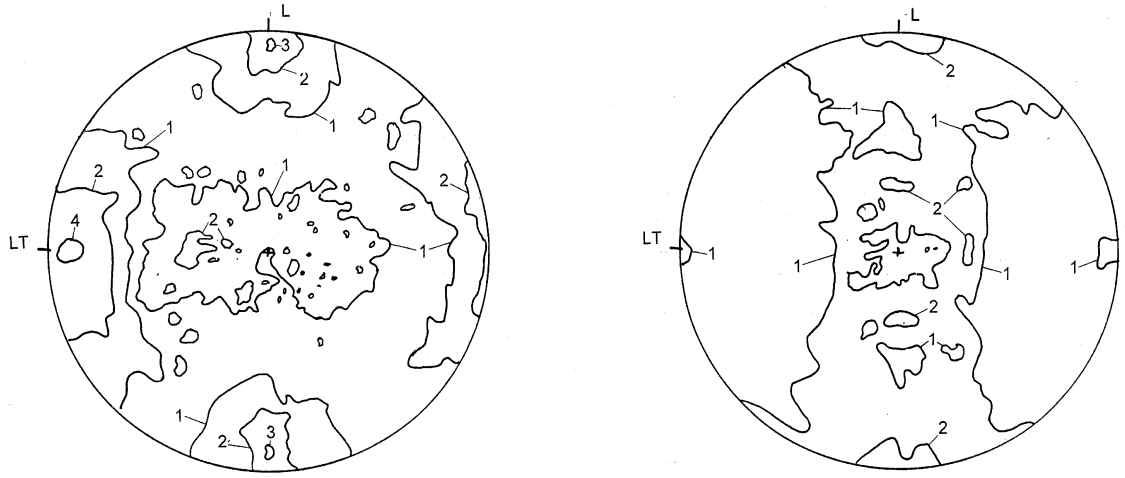

Fig. 2 – Crystallographic texture of the forged Ti-6Al-4V shown as pole figures. Numbers represent the ratio of the intensities of the (a) (0002) basal planes and (b) $\{10\bar{1}0\}$ prismatic planes of the hexagonal closed packed α phase to that of the random texture of the hot isostatic pressed powder standard.

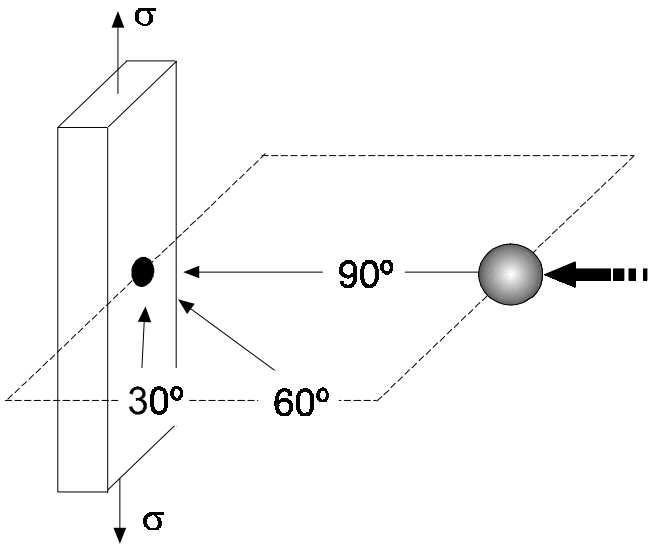

Fig. 3 – Schematic illustration showing impact angles with respect to specimen geometry and loading axis for fatigue tests. In this study, a normal (90°) impact angle was chosen.

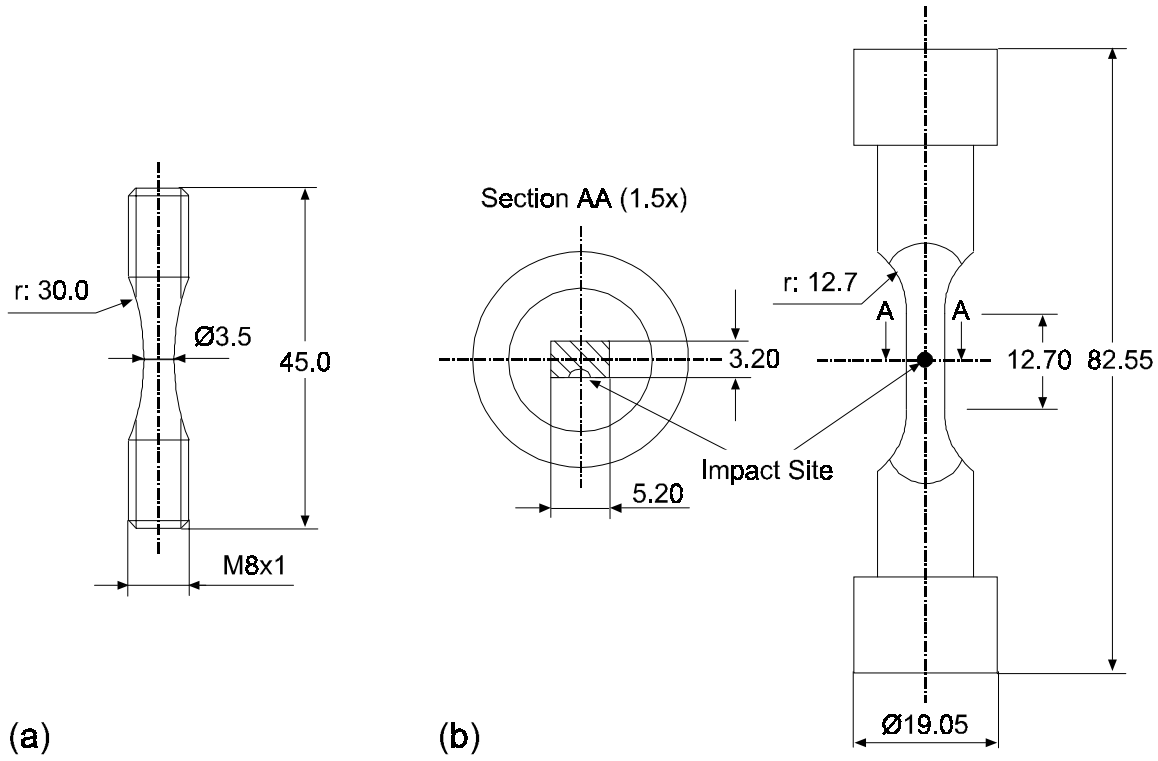

Fig. 4 – Drawings of the specimen geometries used, showing (a) smooth-bar specimen for S-N curves, and (b) modified K_B specimen for simulated FOD studies. All dimensions are in mm.

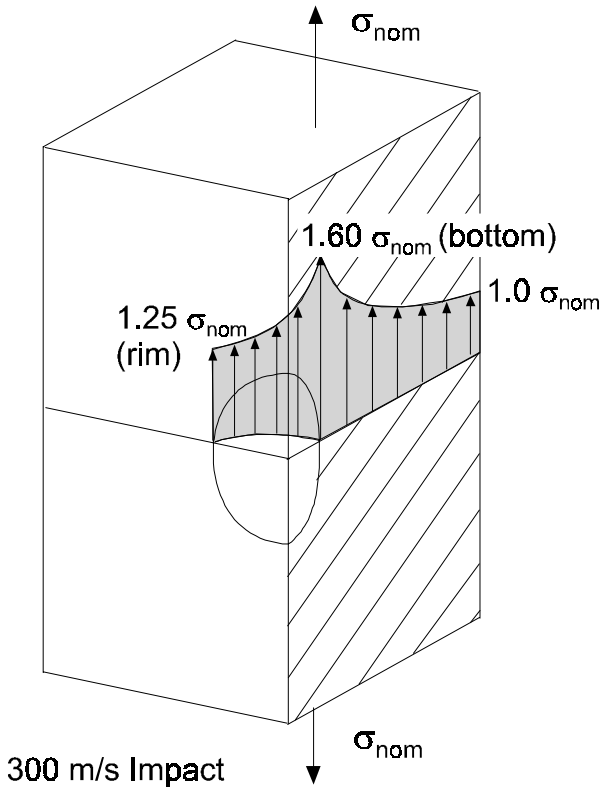

Fig. 5 – Schematic illustration showing the stress concentration surrounding a FOD indentation crater (based on Nisida *et al*.[35]).

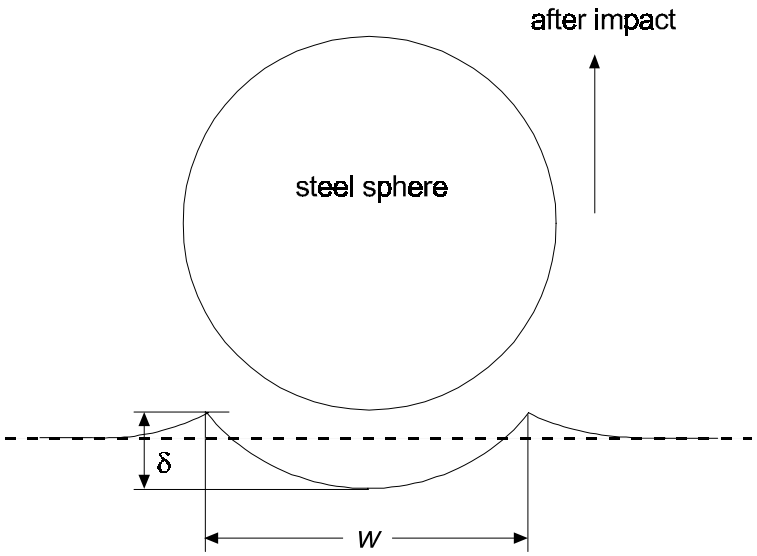

Fig. 6 – Schematic illustration of the cross section of simulated FOD crater after impact. (W is the chord width, δ is the depth).

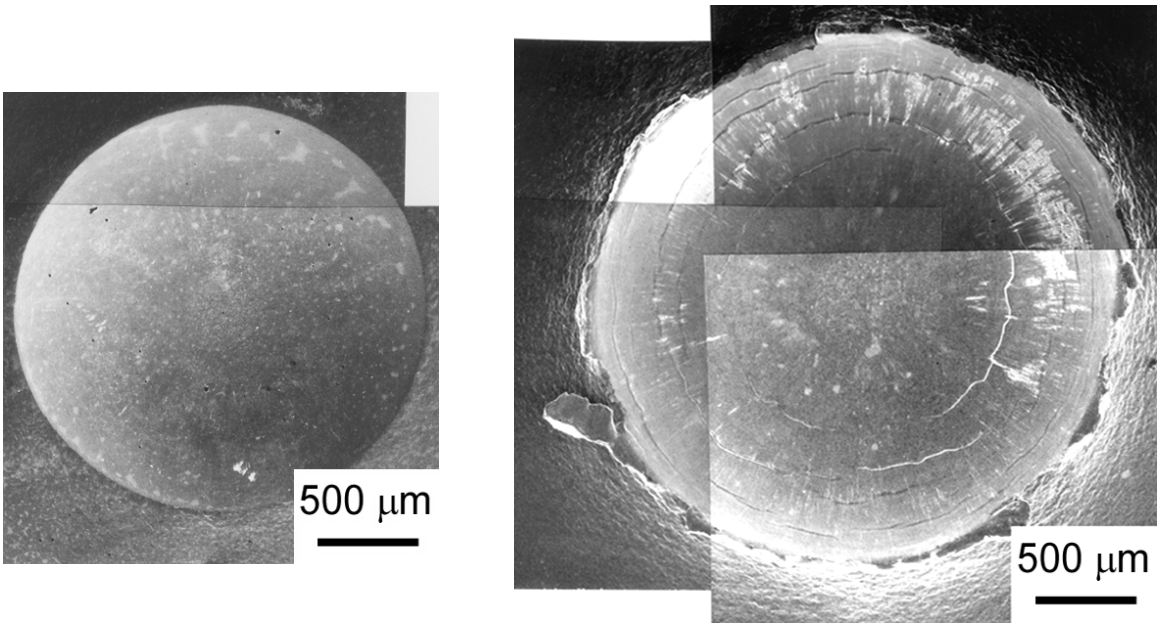

Fig. 7 – Scanning electron micrograph of impact damage sites for (a) 200 m/s and (b) 300 m/s impact velocities, indicating increasing damage with increasing velocity with respect to indentation size, ip formation at crater rim and intense shear band formation emanating at the indent surface.

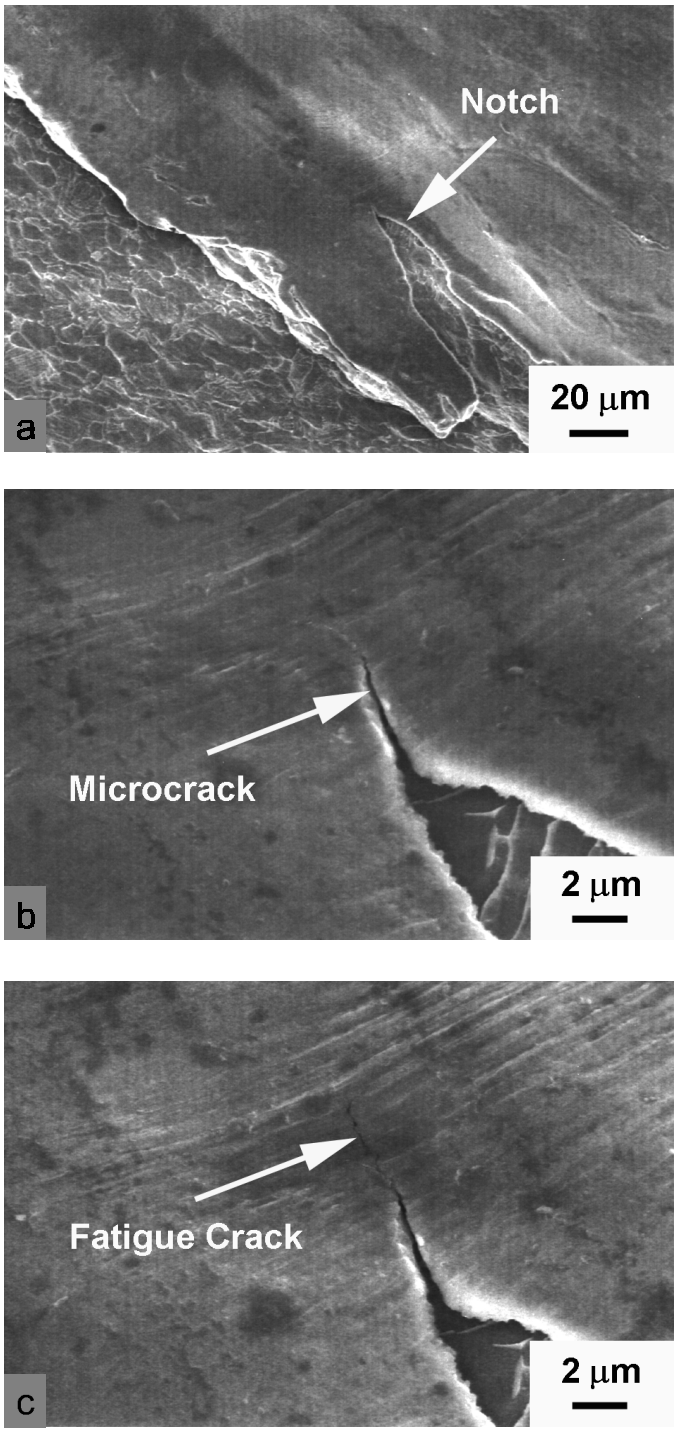

Fig. 8 – Scanning electron micrographs showing the presence of microcracking at crater rim of a FOD indent after the highest velocity (300 m/s) impacts. Micrographs show (a) local notches at crater rim caused by plastic flow of material, (b) microcracks emanating from such notches, and (c) subsequent fatigue-crack growth initiated at such microcracks after 5000 cycles at σ_{max} = 500 MPa (R=0.1).

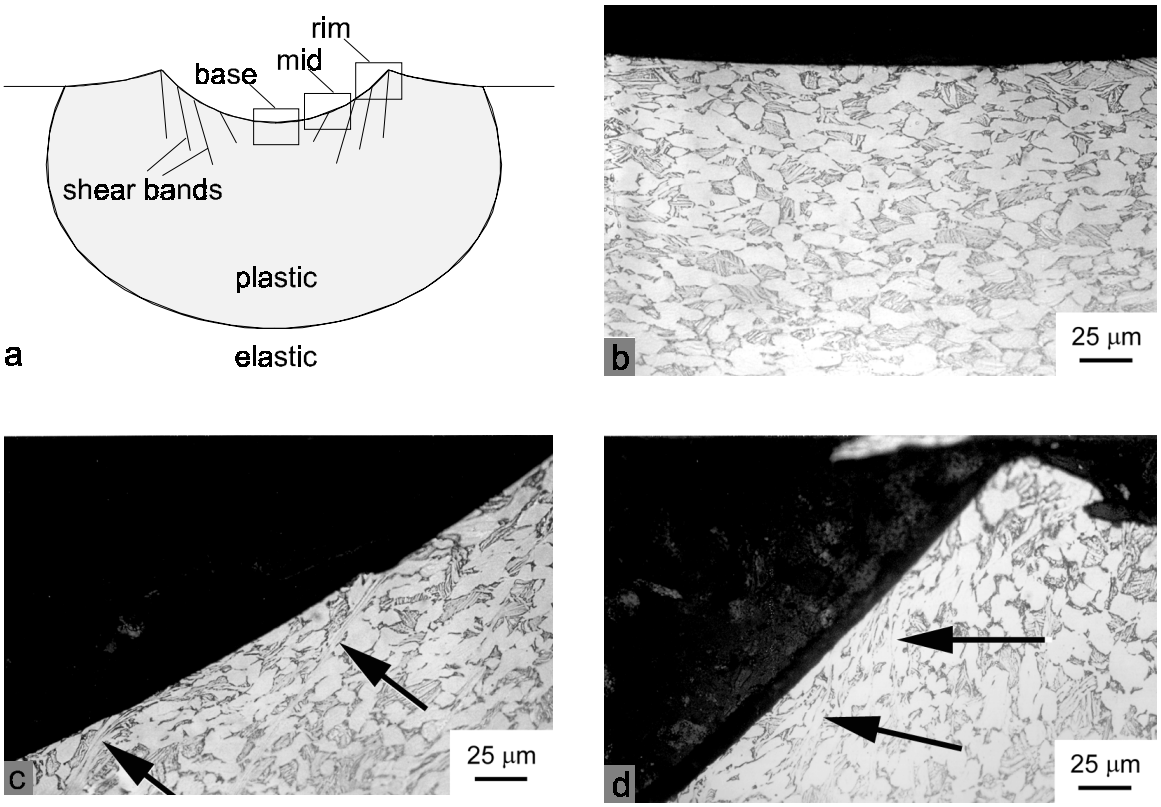

Fig. 9 – FOD following 300 m/s impacts, showing (a) schematic of the crater, and optical micrographs of cross sections at (b) the base, (c) mid location, and (d) rim of the crater. Note formation of shear bands emanating from the surface at mid and rim positions (marked by arrows).

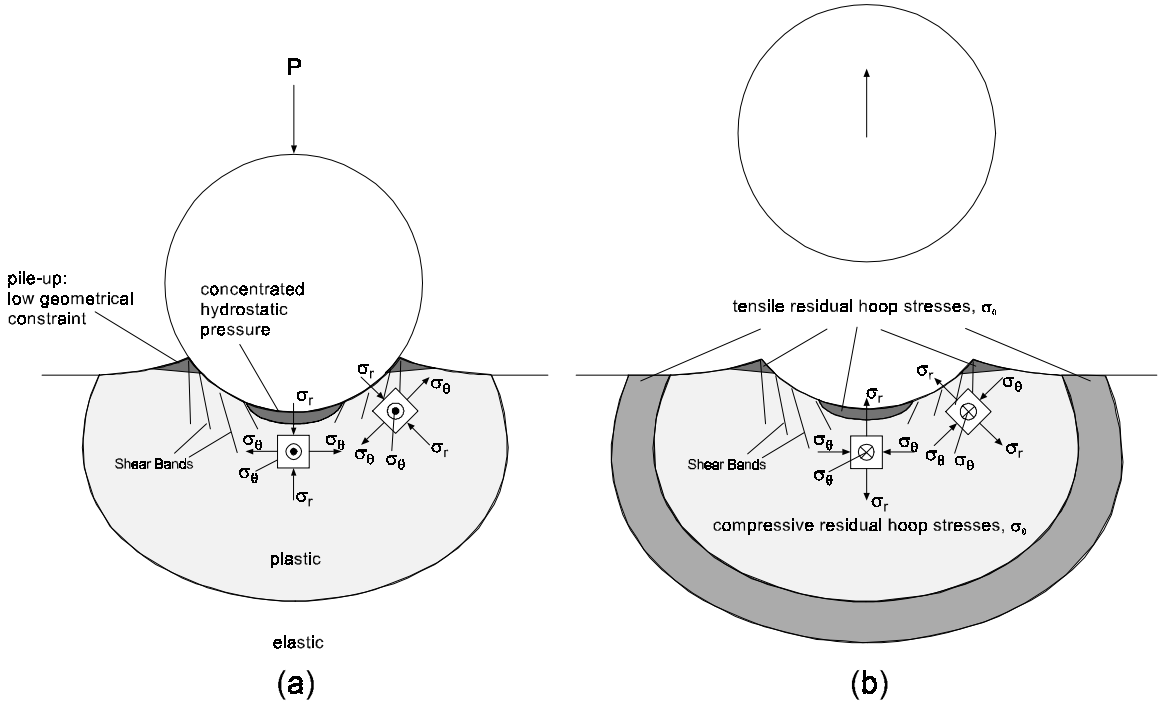

Fig. 10 – Model of high-velocity impact loading and resulting residual stress state, showing (a) state of stress at impact loading, and (b) state of residual stresses after impact loading (σ_r = radial stress, σ_θ = hoop stress).

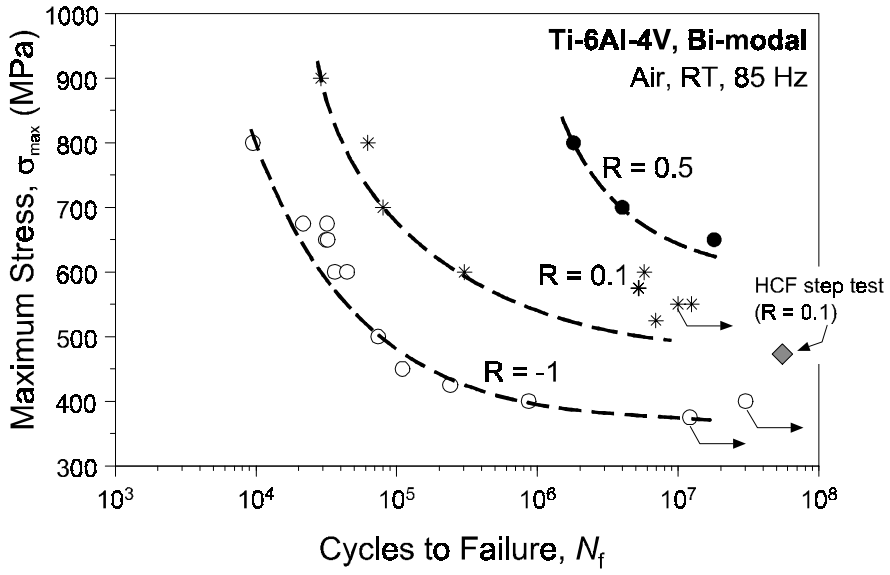

Fig. 11 – Stress-life (S-N) curves for bimodal Ti-6Al-4V, determined using smooth-bar specimens.[41] Also shown is the result of HCF step test at R = 0.1, based on modified K_B specimen testing.

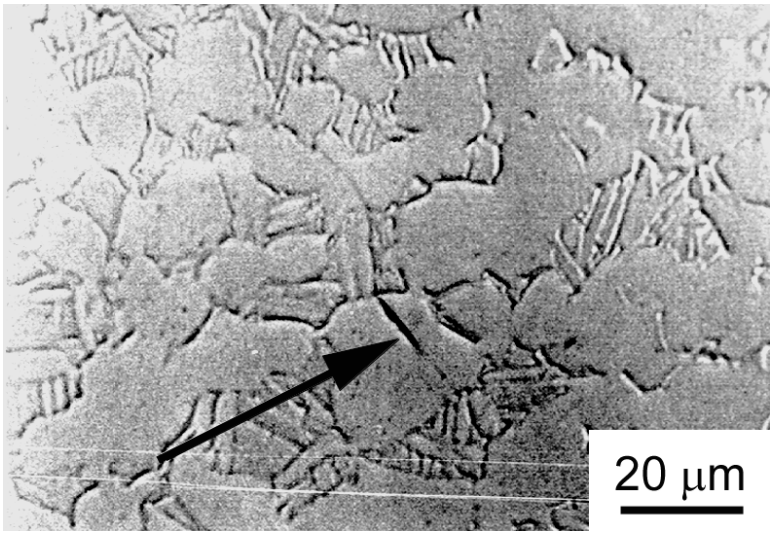

Fig. 12 – Optical micrograph showing surface crack initiation within a globular phase (R=-1, σ_{max} = 650 MPa, $N_F = 1 \times 10^4$ cycles).[41]

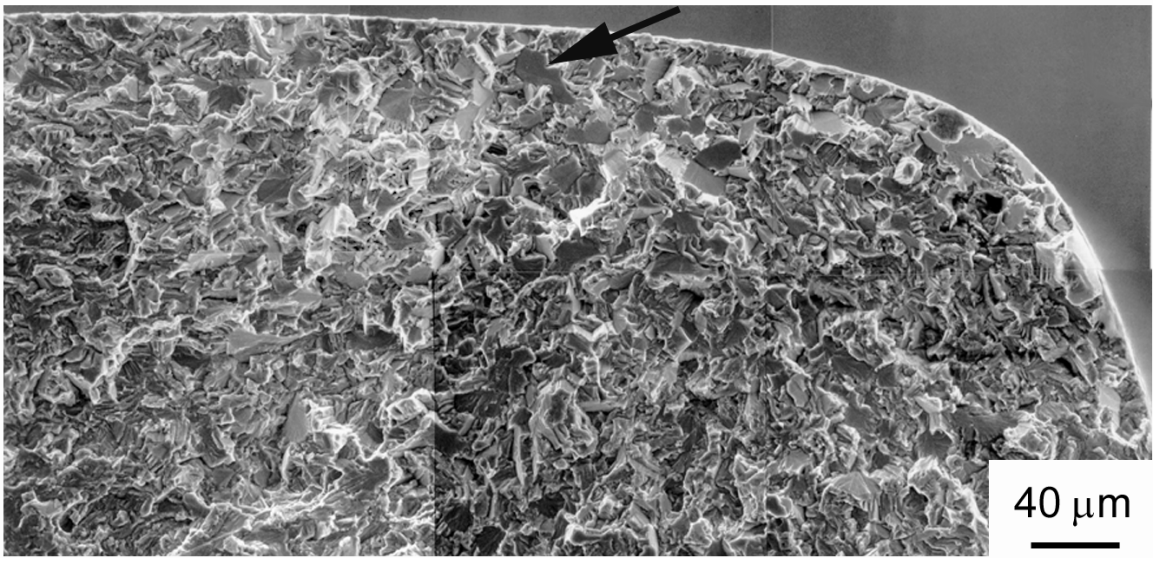

Fig. 13 – Scanning electron micrograph showing subsurface crack initiation (see arrow) on a fatigue fracture surface of a modified K_B specimen (HCF step test at $R = 0.1$, σmax = 475 MPa, $N_F = 5.3 \times 10^7$ cycles).

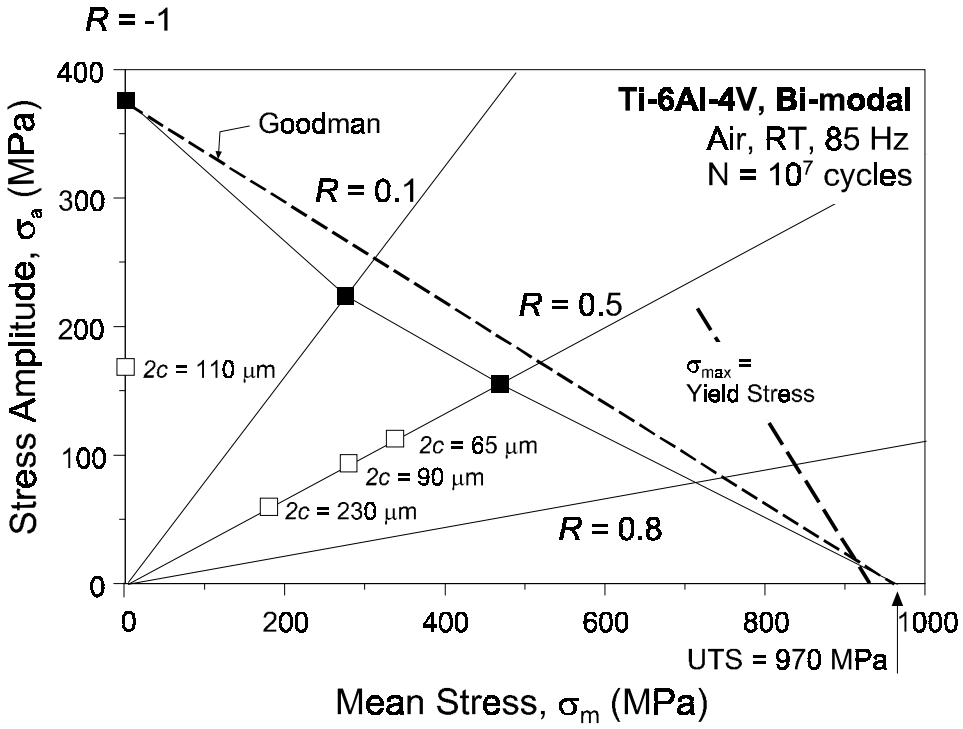

Fig. 14 – Modified Goodman diagram showing the mean and alternating stress to give a life of $N_F = 1 \times 10^7$ cycles in bimodal Ti-6Al-4V, based on smooth-bar specimen tests (closed symbols). Also shown are data for the small-crack HCF threshold testing at $\Delta K = 1.5$ MPa$\sqrt{m}$ tests (open symbols).

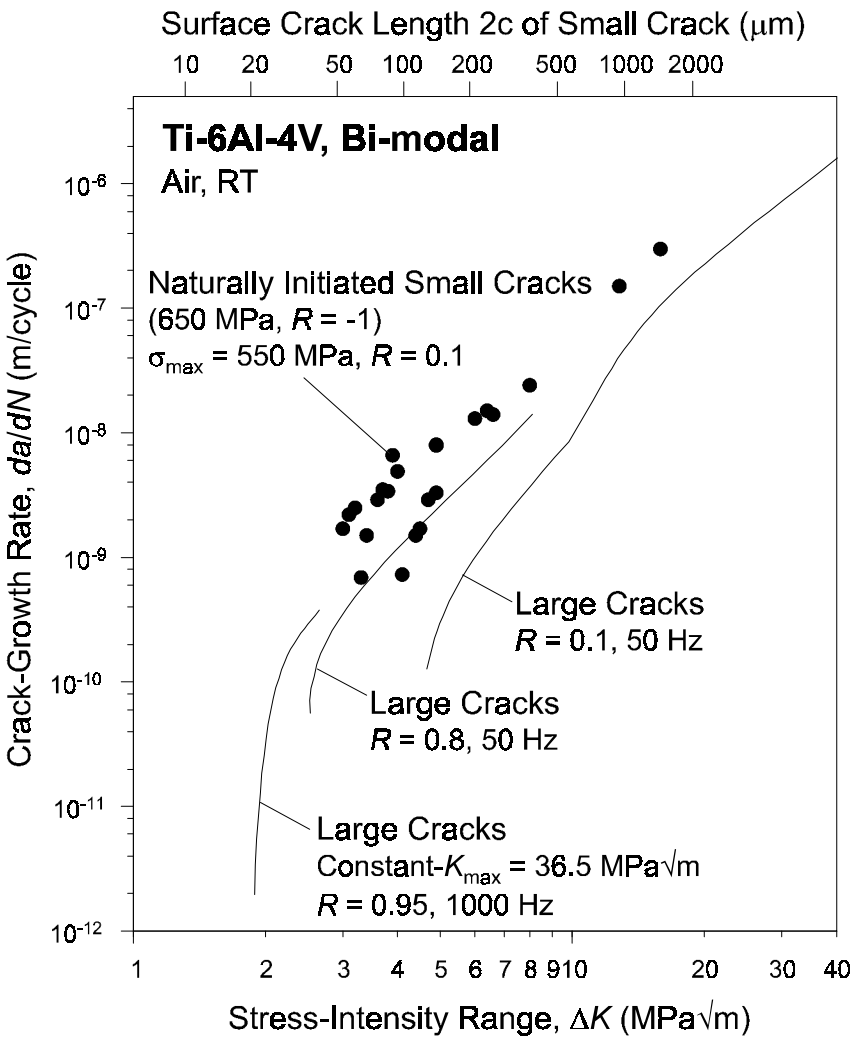

Fig. 15 – Variation in crack-growth rates, *da/dN*, with the applied stress-intensity range, ΔK, for naturally-initiated small cracks (~45 to 1000 μm)[41] and through-thickness large cracks (>5 mm) in bimodal Ti-6Al-4V. Small cracks were initiated at σ_{max} = 650 MPa (R = -1). Large-crack growth data for $R \leq 0.8$ were derived from constant load-ratio tests, whereas for $R \geq 0.8$, constant-K_{max}/increasing-K_{min} testing was used.

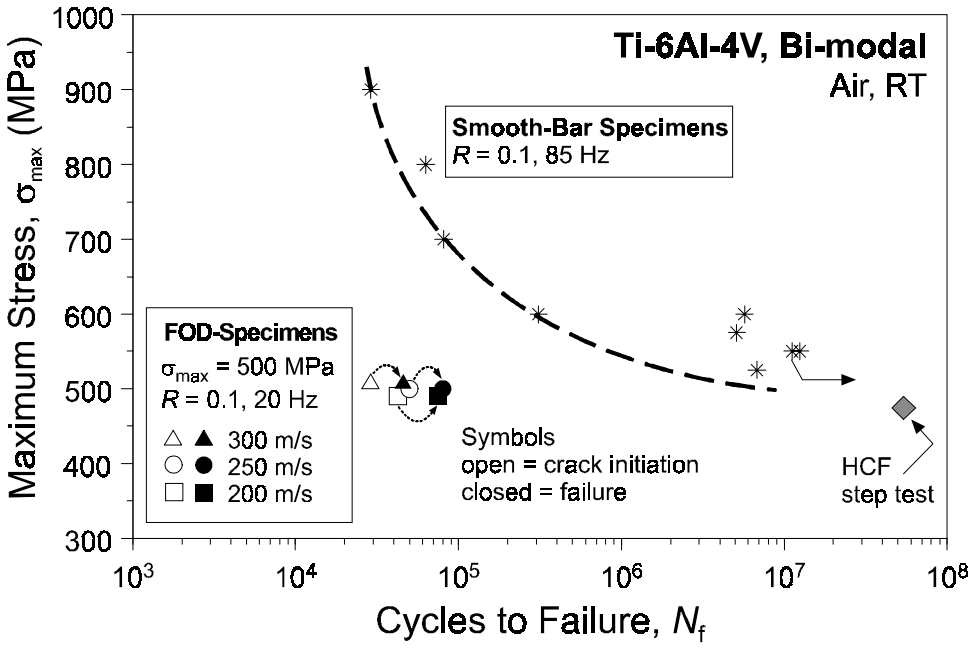

Fig. 16 – The effect of FOD on the S-N data for bimodal Ti-6Al-4V, showing sharply reduced lifetimes. In addition, the result of the HCF step test at R = 0.1 is shown for smooth modified K_B specimen.

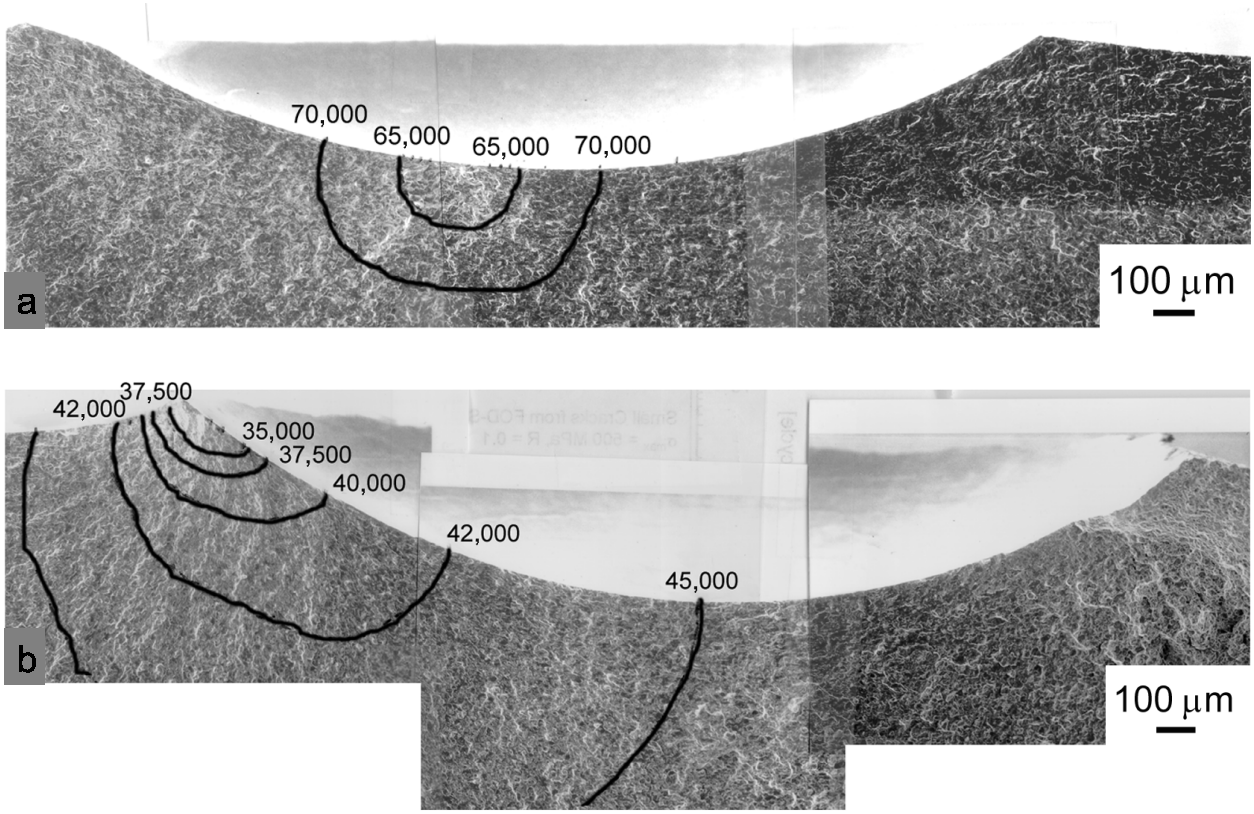

Fig. 17 – Scanning electron micrographs showing the growth of fatigue cracks initiated at FOD impact sites. The progressive position of the crack front is marked on the fracture surface to indicate the initiation sites and crack shapes during crack extension for (a) 250 m/s impact, and (b) 300 m/s impact.

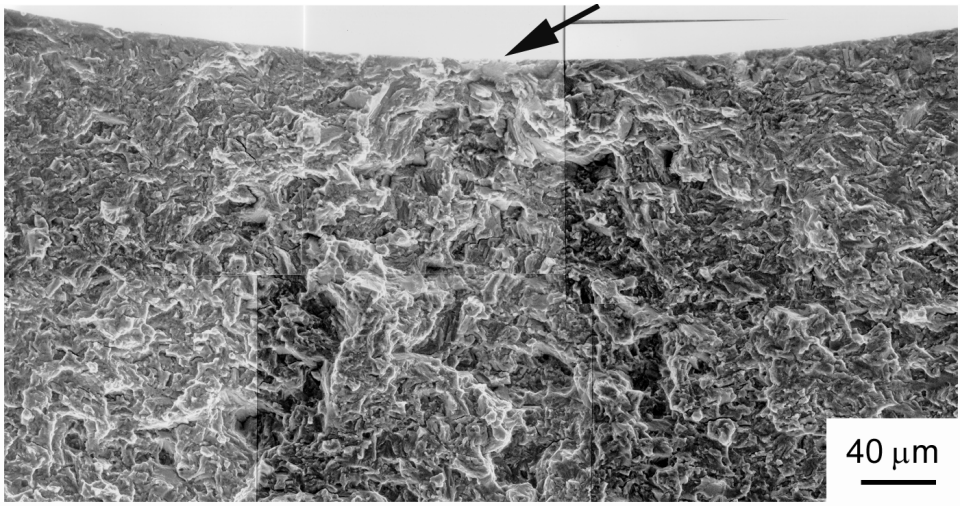

Fig. 18 – Scanning electron micrograph of the fracture surface following fatigue of a 250 m/s FOD impacted K_B specimen, showing surface crack initiation (marked by the arrow) at the base of the indent (σ_{max} = 500 MPa, R = 0.1, $N_F = 7.9 \times 10^4$ cycles).

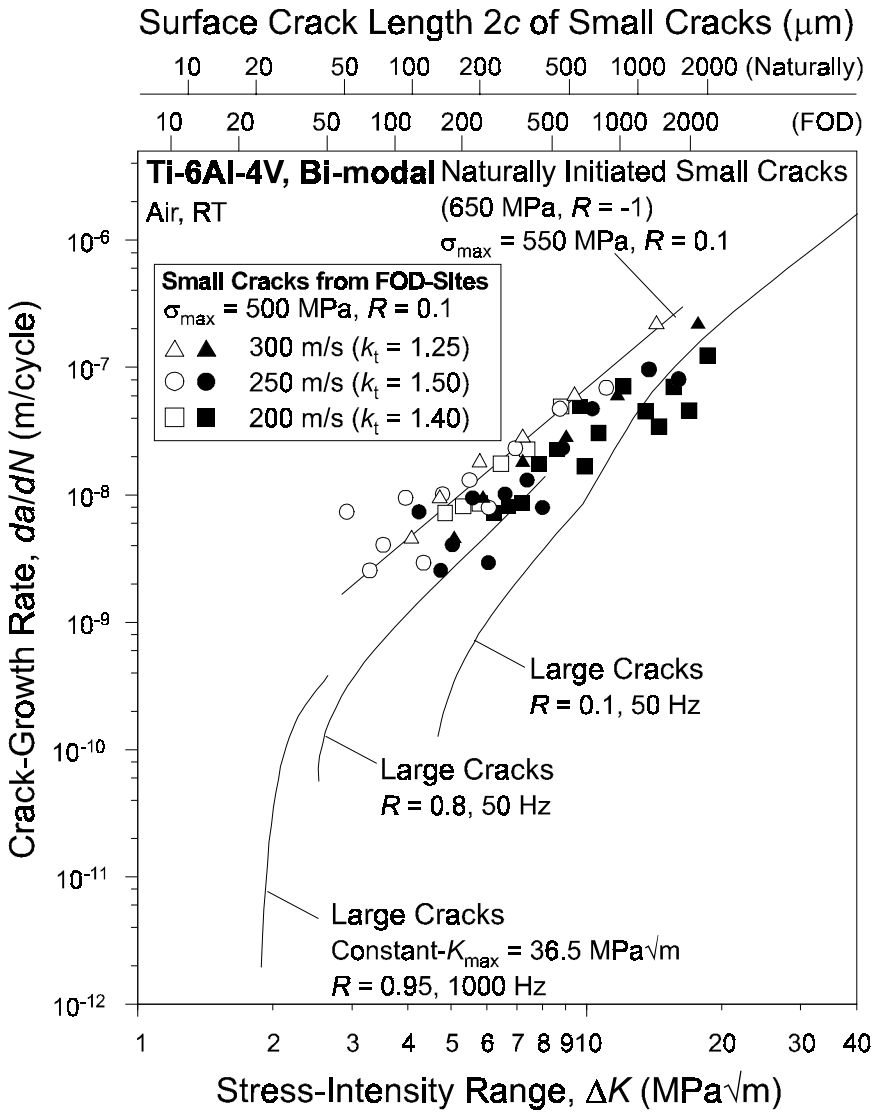

Fig. 19 – Comparison of the variation in crack-growth rates, *da/dN*, with the applied stress-intensity range, ΔK, for FOD-initiated small cracks (~45 to 1000 μm) with that for naturally initiated small cracks[41] and through-thickness large cracks in bimodal Ti-6Al-4V. Stress intensity data for FOD initiated crack growth has been corrected for the stress concentration associated with the indent using the *K* solution of Lukas[36] and stress-concentration factors from Nisida *et al*.[35] (closed symbols); non-corrected data are shown for comparison (open symbols).